System mass constraints for the accreting millisecond pulsar XTE J1814-338 using Bowen fluorescence

L. Wang,[1]★ D. Steeghs,[1]★ J. Casares,[2,3,4] P. A. Charles,[5,6] T. Muñoz-Darias,[2,3] T. R. Marsh,[1] R. I. Hynes[7] and K. O'Brien[4]

[1]*Department of Physics, University of Warwick, Gibbet Hill Road, Coventry CV4 7AL, UK*
[2]*Instituto de Astrofísica de Canarias, 38205 La Laguna, Tenerife, Spain*
[3]*Departamento de astrofísica, Univ. de La Laguna, E-38206 La Laguna, Tenerife, Spain*
[4]*Department of Physics, Astrophysics, University of Oxford, Denys Wilkinson Building, Keble Road, Oxford OX1 3RH, UK*
[5]*Department of Physics and Astronomy, University of Southampton, Southampton SO17 1BJ, UK*
[6]*Astrophysics, Cosmology and Gravity Centre (ACGC), University of Cape Town, Private Bag X3, Rondebosch, 7701, South Africa*
[7]*Department of Physics and Astronomy, Louisiana State University, Baton Rouge, LA 70803, USA*

ABSTRACT

We present phase-resolved spectroscopy of the millisecond X-ray pulsar XTE J1814-338 obtained during its 2003 outburst. The spectra are dominated by high-excitation emission lines of He II $\lambda 4686$, Hβ, and the Bowen blend C III/N III 4630–50 Å. We exploit the proven Bowen fluorescence technique to establish a complete set of dynamical system parameter constraints using bootstrap Doppler tomography, a first for an accreting millisecond X-ray pulsar binary. The reconstructed Doppler map of the N III $\lambda 4640$ Bowen transition exhibits a statistically significant ($>4\sigma$) spot feature at the expected position of the companion star. If this feature is driven by irradiation of the surface of the Roche lobe filling companion, we derive a strict lower limit to the true radial velocity semi-amplitude K_2. Combining our donor constraint with the well-constrained orbit of the neutron star leads to a determination of the binary mass ratio: $q = 0.123^{+0.012}_{-0.010}$. The component masses are not tightly constrained given our lack of knowledge of the binary inclination. We cannot rule out a canonical neutron star mass of 1.4 M$_\odot$ (1.1 M$_\odot$ < M_1 < 3.1 M$_\odot$; 95 per cent). The 68/95 per cent confidence limits of M_2 are consistent with the companion being a significantly bloated, M-type main-sequence star. Our findings, combined with results from studies of the quiescent optical counterpart of XTE J1814-338, suggest the presence of a rotation-powered millisecond pulsar in XTE J1814-338 during an X-ray quiescent state. The companion mass is typical of the so-called redback pulsar binary systems ($M_2 \sim 0.2$ M$_\odot$).

Key words: accretion, accretion discs – binaries: close – stars: individual: XTE J1814-338 – X-rays: stars.

1 INTRODUCTION

Low-mass X-ray binaries (LMXBs) are systems in which a neutron star (NS) or a black hole accretes matter from a low-mass companion star. Since the discovery of the first millisecond radio pulsar (MSP; Backer et al. 1982), it has been suspected that long periods of mass transfer on to old NSs hosted in LMXBs might be responsible for spinning up the compact object to the ms regime. A 'recycled' MSP is thought to be formed when accretion turns off completely (Alpar et al. 1982). The detection of the first accreting millisecond

X-ray pulsar (AMXP) SAX J1808.4-3658 in the course of an X-ray outburst episode (Wijnands & van der Klis 1998) provided a nice confirmation of the recycling scenario. The radio pulsar/LMXB link was firmly confirmed with more recent discoveries of transitional millisecond pulsar binaries. The most notable examples include the 'missing link pulsar' PSR J1023+0038 that turned on as an MSP after an LMXB phase (Archibald et al. 2009); and the direct evolutionary link IGR J18245-2452, which has shown both an MSP and an AMXP phase (Papitto et al. 2013); and XSS J1227.0-4859 (see e.g. de Martino et al. 2014; Roy et al. 2015).

The fifth AMXP XTE J1814-338 was discovered on 2003 June 5 by the *Rossi X-ray Timing Explorer* satellite during routine observations of the Galactic-centre region, and has a pulse frequency of 314 Hz (Markwardt & Swank 2003). Among the ~15 known

★ E-mail: Zhuqing.Wang@warwick.ac.uk (LW); D.T.H.Steeghs@warwick.ac.uk (DS)

AMXP systems (see Patruno & Watts 2012 for a recent review), its 4.3 h orbital period is the most similar to the period of 'classic' non-pulsing NS LMXBs, e.g. 4U 1735-444 (4.7 h), GX 9+9 (4.2 h) or 4U 1636-536 (3.8 h). A total of 28 type I X-ray bursts have been observed from XTE J1814-338 to date, all with burst oscillations in the vicinity of the 314 Hz pulsar frequency, confirming that the burst oscillation frequency for XTE J1814-338 is at the NS spin frequency (see e.g. Watts, Strohmayer & Markwardt 2005). A source distance of 8 ± 1.6 kpc was inferred from the last burst which likely reached the Eddington luminosity (Strohmayer et al. 2003).

The presence of ms pulsations provides the opportunity for a precise determination of the orbit of the NS (Papitto et al. 2007). However, in order to establish a complete set of system parameters, including the mass of the NS, the radial velocity (RV) curve of the companion is required. Optical and near-infrared observations of AMXPs in quiescence can offer promising opportunities to constrain the RV of the donor, as the faint donor star may be detected directly. But so far, these have only led to upper limits or a counterpart that is too faint on which to perform RV studies (e.g. Homer et al. 2001; Jonker et al. 2003; Krauss et al. 2005).

A different avenue for determining system parameters of LMXBs and/or AMXPs in active states was opened up by Steeghs & Casares (2002). High-resolution, phase-resolved blue spectroscopy of the prototypical LMXB Scorpius X-1 revealed extremely narrow, high-excitation emission components arising from the surface of the donor star, leading to the first RV curve for the mass donor in Sco X-1 and binary parameter constraints in support of the presence of a 1.4 M$_\odot$ NS. These narrow emission lines were strongest in the Bowen region (4630–4650 Å) consisting of a blend of N III and C III lines, and are the result of fluorescence of the gas by UV photons from the hot inner disc (McClintock, Canizares & Tarter 1975). This technique has been used to constrain the orbital parameters of a number of persistent LMXBs (see Cornelisse et al. 2008 for a review) as well as transient systems during their outbursts, e.g. GX 339-4 (Hynes et al. 2003) and SAX J1808.4-3658 (Cornelisse et al. 2009).

In this study, we present medium-resolution blue spectroscopy of the accretion-driven millisecond pulsar XTE J1814-338 obtained with the Very Large Telescope (VLT) during its 2003 outburst. The Bowen fluorescence technique is revisited and applied to XTE J1814-338 to establish dynamical system parameter constraints, which can offer insights into the evolutionary scenario involving binary pulsars. Section 2 summarizes the observing strategy and data reduction steps. In Section 3, we present the average spectrum and main emission-line parameters, while RVs of emission lines are presented in Section 4. In Section 5, we exploit the Doppler tomography technique and further develop our methodology to obtain robust binary parameter constraints. Estimation of component masses and discussion of the results are given in Section 6.

2 OBSERVATIONS AND DATA REDUCTION

We observed XTE J1814-338 (hereafter, J1814) using the FORS2 Spectrograph attached to the 8.2m Yepun Telescope (UT4) at Observatorio Monte Paranal [European Southern Observatory (ESO)] on the night of 2003 June 23 (programme 071.D-0372). A total of 20 spectra were obtained with the R1400V holographic grating, covering a complete orbital cycle using 700 s long exposures. Matching with an 0.7 arcsec slit width resulted in a wavelength coverage of 4514–5815 Å at 70 km s^{-1} (full width at half-maximum, FWHM) resolution. The seeing was variable between 0.6 and 1.2 arcsec during our run. The slit position angle was fixed to PA = 100° that

coincides with the parallactic angle at the end of our run, when the airmass of the target was highest (sec $z = 2.1$). At the same time, two comparison stars were included in the slit, which enabled us to monitor slit losses and obtain a relative flux calibration. The flux standard Feige 110 was also observed with the same instrumental configuration to correct for the instrumental response of the detector.

The images were de-biased and flat-fielded, and the spectra were subsequently extracted using conventional optimal extraction techniques in order to optimize the signal-to-noise ratio (SNR) of the output (Horne 1986). A He+Ne+Hg+Cd comparison lamp image was obtained in the daytime to provide the wavelength calibration scale. A fourth-order polynomial fit to 19 arc lines produced an rms scatter < 0.05 Å with a mean dispersion of 0.64 Å pix^{-1}. Instrumental flexure was monitored through cross-correlation between the sky spectra and was found to be very small (always within 5 km s^{-1}). These velocity drifts were nevertheless removed from each individual spectra, and the zero-point of the final wavelength scale was established by the strong O I sky line at 5577.338 Å. Individual spectra were corrected for slit losses using the brighter comparison star that shared the slit with our target. Correction factors were computed using a low-order spline fit to the ratio between each comparison star spectrum and its grand sum average. The target spectra were then divided by these fits to correct for time-dependent slit losses.

3 AVERAGE SPECTRUM AND ORBITAL VARIABILITY

The average spectrum of J1814 is presented in Fig. 1. The spectrum is dominated by high-excitation emission lines of He II λλ4686, 5411 Å, the Bowen blend at λλ4630–50 and Hβ, which are typical of LMXBs and Soft X-ray Transients in outburst and first noted in Steeghs (2003b). He I lines at λ4922 and λ5015 are significantly weaker and no absorption components are discernible in the Balmer or He I lines, as seen in high-inclination systems such as X1822-371 (see Casares et al. 2003). The He II profiles are double-peaked, as expected from an accretion disc, but the blue peak is considerably stronger than the red peak. The Hβ profile is more complex and its blue side peaks at lower velocities. A list of time-averaged emission-line parameters is presented in Table 1.

Fig. 2 displays the orbital evolution of the most intense emission features presented in 15 phase bins. Binary phases were computed using the extremely accurate X-ray pulsar orbital solution (Papitto et al. 2007) :

$$T_0 \text{ HJD(UTC)} = 2452798.3539536(9) + 0.178110219(2) \text{ E.} \quad (1)$$

Here we adjusted T_0 such that phase 0 corresponds to the inferior conjunction of the companion star in a heliocentric UTC time system. He II λ4686 shows a clear double-peaked profile with the blue peak stronger around phase ~0.6. An S-wave is visible, crossing from blue to red velocities at phase ~0.9. The Hβ profiles are dominated by the blue peak throughout the orbit whereas the Bowen blend is too noisy to directly reveal any multicomponent structure in the raw data. In general, the line intensities appear to peak in flux around phase ~0.3–0.8.

4 RVs AND THE SYSTEMIC VELOCITY

The broad disc emission features may be used to derive RV curves as the disc gas should trace Keplerian orbits around the NS. In order to avoid contamination from line core components (see Fig. 2), we have applied the well-established double-Gaussian technique
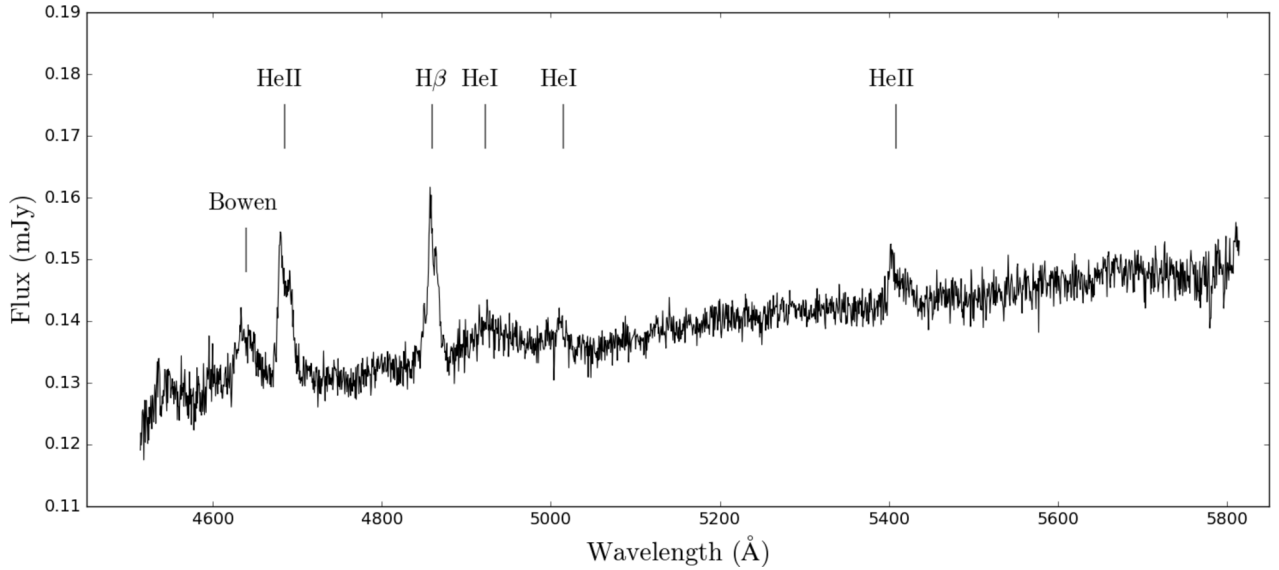
Figure 1. The average optical spectrum of XTE J1814-338. Main emission lines are indicated.
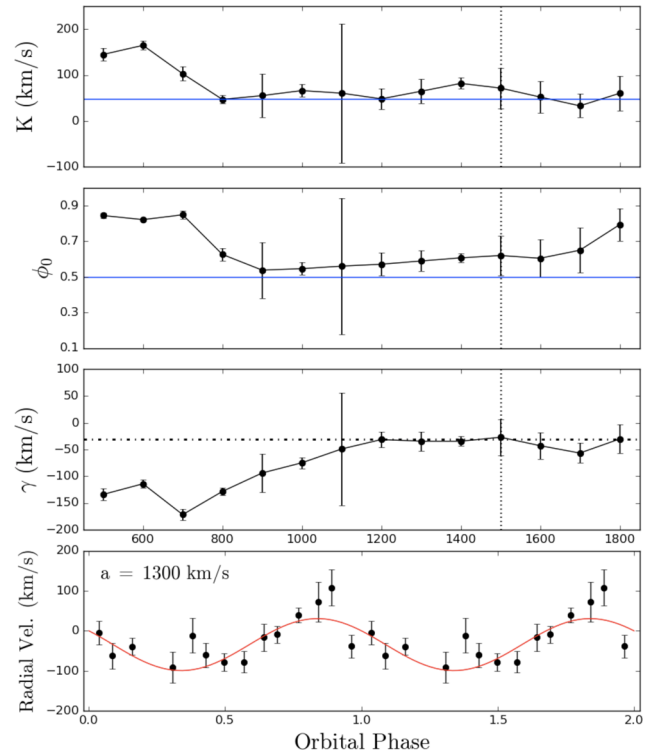
Table 1. Emission-line parameters.

Line	Centroid (Å)	FWHM (km s^{-1})	EW (Å)
Bowen	4639.0 ± 0.8	1613 ± 180	2.2 ± 0.2
He II	4684.6 ± 0.4	1160 ± 70	2.9 ± 0.2
Hβ	4859.7 ± 0.3	920 ± 60	2.8 ± 0.2
He II	5408.5 ± 1.7	1190 ± 200	0.8 ± 0.2
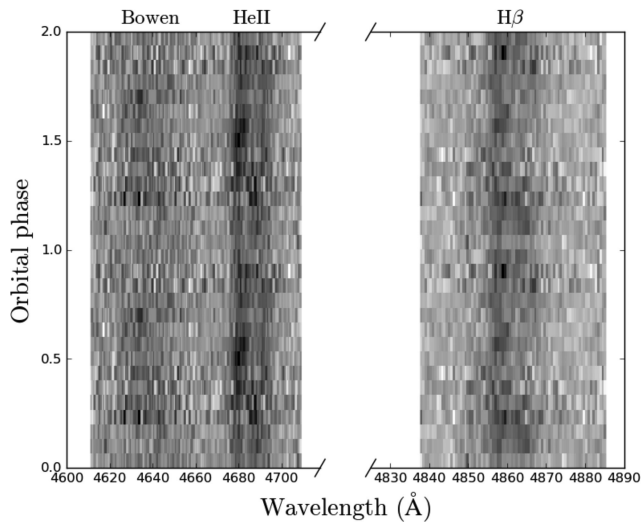
Figure 2. Trailed spectra showing the orbital evolution of the strongest emission lines in 15 phase bins.

Figure 3. The diagnostic diagram of He II λ4686 (top three panels). Fitted sine-wave parameters (with 1σ errors) are plotted as functions of the Gaussian separation a. The vertical dotted line denotes a limit of the Gaussian separation above which the continuum noise dominates the RVs. The bottom panel shows the RV curve for $a = 1300 \, \mathrm{km \, s^{-1}}$ overplotted with the best-fitting sine wave (red curve).

(Schneider & Young 1980) to He II λ4686. The Gaussian widths were fixed to FWHM = 200 km s^{-1} with a variable separation $a =$ 500–1800 km s^{-1} in steps of 100 km s^{-1}. The RV curves were fitted with a sine function and the resultant parameters are displayed using the traditional diagnostic diagram (Fig. 3; Shafter 1985). As we move away from the line core and thus mainly probe the dynamics of the inner disc gas, the γ-velocity stabilizes towards -30 km s^{-1} (horizontal dash–dotted line). The RV amplitude K drops from $\sim$150

to 50 km s^{-1} and the phasing decreases from $\sim$0.85 to 0.5–0.6. From the pulsar solution, we know the absolute phase (0.5) and velocity semi-amplitude of the NS ($K_{\mathrm{I}} = 47.848 \pm 0.001$ km s^{-1}, marked as horizontal blue lines in Fig. 3). It thus appears that in the range $a \sim 900$–1200 km s^{-1}, the disc dynamics tracks the true orbit of the NS quite well. At larger separations, parameters deviate again

due to increasing noise as we probe the faint line wings. Although we know K_1 already, this estimate suggests a systemic velocity near $-30 \, \text{km s}^{-1}$. In the next section, we present an alternative derivation of the systemic velocity (see Section 5.3.1) using a new methodology, to be compared with the more traditional double Gaussian probe.

5 ANALYSIS

5.1 Doppler mapping

The discovery of narrow, high-excitation Bowen emission lines arising from the irradiated donor star in Sco X-1 opened up a new window to achieve robust RV studies in luminous LMXBs (Steeghs & Casares 2002). Only in very few cases was it possible to use the conventional RV fitting method. For nearly all the fainter sources, the use of Doppler tomography-based methods was required in order to detect Bowen emission from the donor at low SNRs (S/N < 10).

The Doppler tomography technique essentially uses all input spectra at once (ideally covering a whole orbital period) to invert phase-resolved data into an equivalent image of brightness distribution in velocity space or Doppler coordinates (Marsh & Horne 1988). This approach is well suited for faint donor components and has the advantage of being able to separate various sources of emission nicely in the output velocity-space image. In the Doppler coordinate frame, the V_x-axis is defined by the direction from the accreting compact object to the donor star; the V_y-axis points in the direction of motion of the donor. If the input γ parameter is close to the true systemic velocity, the origin at $(V_x, V_y) = (0, 0)$ should then correspond to the centre of mass of the system. The transformation preserves the shape of the Roche lobe, and donor emission will always be mapped to a compact spot on the positive V_y-axis (provided that the correct ephemeris is used). If a Bowen spot is found at the expected position of the donor in the reconstructed tomogram, the (apparent) RV semi-amplitude (K_{em}) of the secondary can be measured accurately from the map through a 2D Gaussian fit to the spot region.

For J1814, we first prepared the spectra by subtracting a low-order spline fit to the continuum regions and subsequently used the second generation (PYTHON/C++ based), maximum entropy Doppler tomography code[1] developed by T. Marsh (Manser et al. 2016) to exploit all 20 spectra simultaneously. In Fig. 4, we show the Doppler tomograms of the principal lines seen in our spectra using the ephemeris in equation (1) and $\gamma = -30 \, \text{km s}^{-1}$.

Both He II and Hβ maps show the classic ring-like features corresponding to emission from the accretion disc. An extended bright spot can be seen in the upper left velocity quadrant of these maps, suggesting excited emission from the stream-disc impact region. In addition to evidence of bright spot emission, the map of N III $\lambda4640$ (usually the strongest Bowen component) for J1814 reveals a sharp spot along the positive V_y-axis. The centroid is at the position $V_x \sim -20 \, \text{km s}^{-1}$ and $V_y \sim 319 \, \text{km s}^{-1}$. The shape and phasing of this spot feature suggest that we may have detected a signal from the irradiated companion. Finally, we notice another bright spot at approximately the expected phase of the companion in the He II $\lambda5411$ map; the spot is clearly at a much larger velocity ($V_x \sim 30 \, \text{km s}^{-1}$, $V_y \sim 483 \, \text{km s}^{-1}$) and more extended than the N III $\lambda4640$ spot.
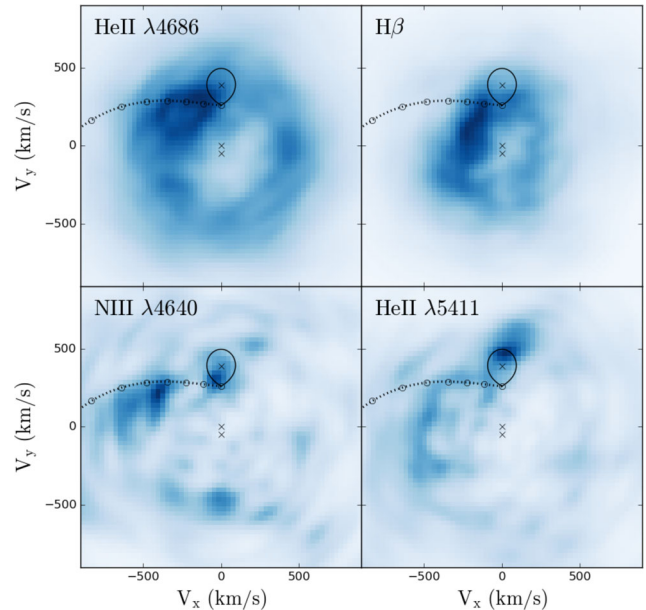
Figure 4. Doppler maps of several spectral features. All images were computed for a systemic velocity $\gamma = -30 \, \text{km s}^{-1}$. We plot the gas stream trajectory and the Roche lobe of the donor star using $K_1 = 47.848 \, \text{km s}^{-1}$ and our best estimate of the mass ratio of 0.123 (see Section 6.2). The centre-of-mass velocity of the mass donor $(0, K_2 = 390 \, \text{km s}^{-1})$, the centre of mass of the system $(0, 0)$ and the velocity of the NS $(0, -K_1)$ are denoted by crosses.

5.2 Bootstrap Monte Carlo

5.2.1 Significance testing

Perhaps the most important step towards robust binary parameter estimation using the Bowen technique involves confirming the statistical significance of any donor star components and to determine their position in velocity space robustly. This becomes increasingly difficult as we push into lower SNR regimes, with correspondingly noisier Doppler maps that may contain spurious features. Therefore, it is vital to test the significance of the features seen in the N III $\lambda4640$ and He II $\lambda5411$ maps of J1814, before carrying out further rigorous analysis based on our reconstructions.

After testing on both synthetic and real data sets, we have opted to use the robust and versatile bootstrap technique to derive estimates of the standard deviation and confidence intervals (CIs) on a real data set with unknown probability distribution function (Watson & Dhillon 2001; Longa-Peña, Steeghs & Marsh 2015). The idea of the bootstrap method is to use the data themselves as an estimator of their underlying parent distribution (Efron & Tibshirani 1993). By randomly selecting from the original data set allowing duplicates, simulated data sets of the same size as the original sample can be created. To allow for approximately the same noise level to be present in the bootstrap data set as in the original data, only the error bars of the observed data were manipulated (see the details in Watson & Dhillon 2001). For each bootstrap data set, we compute a reconstructed image (automated processes; see Section 5.2.2) in the same manner as for the original image.

5.2.2 Monte-Carlo Doppler mapping

Upon creating a large number of new maps by resampling from the original trailed spectra, histograms of spot parameters can be constructed from ensembles of 2D Gaussian fits. The histograms

---

[1] https://github.com/trmrsh/trm-doppler

provide information about the unknown sampling distribution of each property, including the centroid position, peak intensity and FWHM. We can estimate the mean, the variance and confidence regions for any of these properties based on the bootstrap distribution.

We have carefully examined sources of undesirable (random) variations that have high potential to distort the shape of the resulting bootstrap distribution and lead to inaccurate conclusions. While it may seem natural to fit all bootstrap spectra to the same user-defined goodness-of-fit level (χ^2) as the observed spectra, it turns out that for maximum entropy (MEM) Doppler mapping, setting the same reduced χ^2 to aim for can lead to broad entropy distribution across bootstraps, especially in low SNR regimes. This means that in some cases, the bootstrap map looks simpler or smoother than the original map; in other cases, we may end up with much noisier reconstructions, where the code has a hard time to reach the target χ^2 and attempts to fit noise as well as signal. This issue can be resolved by iterating all maps towards constant entropy (S) level, as suggested in Marsh (2001).

For each inversion, we first construct a smooth map by specifying a high initial value of χ^2 and then decrease C_{aim} in small steps until the corresponding entropy reaches the desired value. The grid search is implemented through custom wrapper functions around the new DOPPLER routines. One effectively searches for the optimal MEM solution, so that the realism (measured by χ^2) and simplicity (measured by S) can be ideally balanced for all simulated images. Variation can be further reduced by increasing the size of the computational bootstrap (N_B). We have tested that $N_B \gtrsim 2000$ yields robust results within a reasonable time budget (several hours/days of computation). In the rest of the analysis, all errors and significance levels are calculated from more than 2000 bootstrap samples with maps iterated to reach the same image entropy.

5.2.3 Confirmation of the donor signature

We start by estimating the significance of the most promising feature present in the N III $\lambda4640$ Doppler map as well as the statistical error of the phase shift relative to the pulsar ephemeris (see 5.1). It is known that the choice of the input parameter γ can have an impact on the final Doppler image. In cases of high spectral resolution and high SNRs, an independent estimate of γ can be obtained by reconstructing a series of maps with a range of γs, and searching for the one that yields the best fit to the data (minimal χ^2), as well as an ideal, artefact-free image (Steeghs 2003a).

In the case of J1814, we also generated a series of N III $\lambda4640$ maps with γ varying from -200 to $200\,\mathrm{km\,s^{-1}}$ in steps of $5\,\mathrm{km\,s^{-1}}$, but found no pronounced minimum in χ^2. Reduced χ^2 remained low ($\chi_\nu^2 < 1.4$) for γ between -200 and $30\,\mathrm{km\,s^{-1}}$. Based on this test, we conclude that the systemic velocity is indeed more likely to be negative, but that our SNR is too low to permit us to tightly constrain γ. Among our N III $\lambda4640$ maps, only a subset (γ between -60 and $10\,\mathrm{km\,s^{-1}}$) reveals a sharp, Gaussian-type spot feature along the positive V_y-axis, which we interpreted as a possible donor signature. Thus, we choose to consider all reconstructions within this γ range in the subsequent analysis. To suppress the noise and enhance signal strength, we also created the combined Bowen Doppler maps, for which we included both the N III $\lambda4640$ and the N III $\lambda4634$ components.[2] The combined Bowen map is almost identical in structure with the N III $\lambda4640$ map (see Fig. 4).

---

[2] Relevant Bowen components (other than the N III $\lambda4640$ line) may be identified by creating a trial Doppler-corrected average spectrum in the rest frame of the donor (see Fig. 8).

In Fig. 5, we give examples of histograms, for a $\gamma = -30\,\mathrm{km\,s^{-1}}$ case, representing the bootstrap distribution of three important spot properties obtained from the combined Bowen map.

First, the bootstrap test allowed us to derive a phase shift (with its 1σ statistical error) of $\Delta\phi_{\mathrm{spot}} = -0.007 \pm 0.009$ ($-2.5 \pm 3^\circ.1$) using the centroid position (V_x, V_y). Given that the binary ephemeris is accurately known thanks to the pulsar, we can thus formally demonstrate that the sharp Bowen spot is effectively centred on the V_y-axis, exactly where the donor star should appear.

Secondly, since all the distributions we obtained (see e.g. Fig. 5) were Gaussian, we estimated the mean and 1σ error of the emission peak (and all the other spot parameters) by fitting a Gaussian curve to the histogram plots. The centre of the peak height distribution (0.064 ± 0.015) for $\gamma = -30\,\mathrm{km\,s^{-1}}$ is different from zero at the 4–4.5σ level, indicating a significant detection (99.99 per cent confidence).

It can be shown using the same method that the bright spot in the upper left velocity quadrant is also significant at the 4.4σ level, and likely originates from the stream-disc impact region. A third faint spot occurs on the negative V_y-axis, with a marginal significance level of 3.2σ; the location suggests that it could be part of a broken-ring-like feature corresponding to the accretion disc. The significance levels of the rest of the spots are all below the 2σ threshold. In summary, although several spot-like features are present in the noisy N III $\lambda4640$/combined Bowen maps, only one sharp feature (statistically significant at the $>4\sigma$ level) lies on the positive V_y-axis and thus can be confidently identified as the donor signature in the case of J1814. The availability of a robust absolute ephemeris in this case simplifies the search, but our methodology is appropriate even in cases where such an ephemeris may not be available and thus all statistically significant components need to be considered.

5.3 The Bowen blend diagnostic

Having confirmed that the Bowen emission is produced on the X-ray illuminated front side of the mass donor and that the relevant emission feature is significant at a level higher than 4σ, we aim to use the emission-line diagnostics to obtain robust system parameter constraints. Along with the phase shift and peak emission, we show the distribution of the corresponding apparent RV semi-amplitude K_{em} ($<K_2$) in Fig. 5. By fitting a Gaussian model to the histogram, we obtain $K_{\mathrm{em}} = 313 \pm 26\,\mathrm{km\,s^{-1}}$. Similar analyses were applied to all the other N III $\lambda4640$ and the combined Bowen maps computed using the previously determined range of γ, and the results can be summarized in the form of a 'Bowen diagnostic diagram' (Fig. 6).

5.3.1 Systemic velocity

In the new diagnostic diagram, we plot the phase shift, $\int K_{\mathrm{em}}$ velocity (with 1σ statistical errors) and the significance level of the combined Bowen spot feature as functions of the assumed γ. Due to the low SNR of our data, we did not find a satisfactory γ range that would minimize the reduced χ^2 of a series of reconstructions (sensitivity to γ is weak). Nevertheless, the map reveals a real donor signature, mapped from one or more sharp 'S-wave' component(s) present in the trailed spectra, we can therefore expect that the best estimate of γ would yield the maximum significance of the secondary feature.

From the bottom panel of Fig. 6, it is clear that the significance of the combined Bowen spot is consistently higher than that of the N III
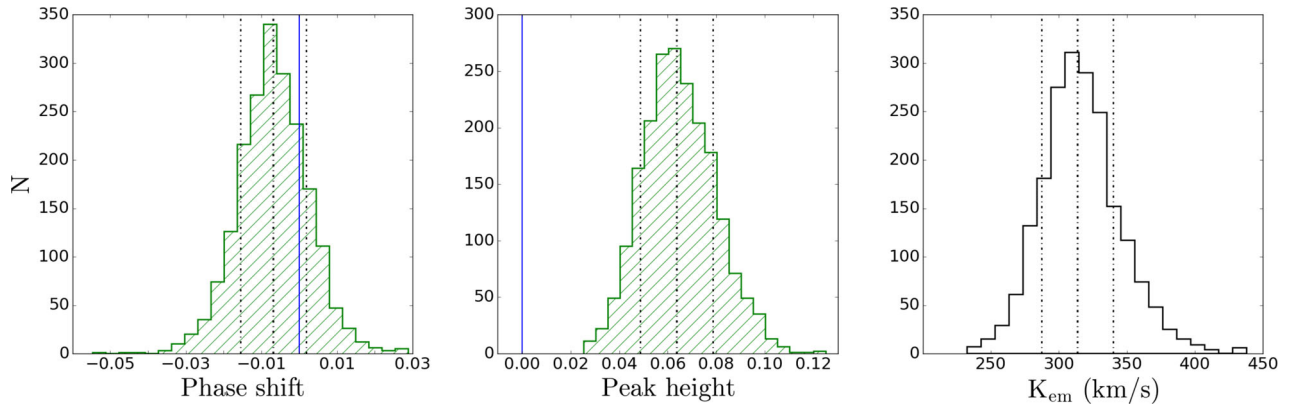
Figure 5. Number distributions of the phase shift (left), peak emission (middle) and RV semi-amplitude (right) measured from 2000 bootstrap maps assuming a systemic velocity of $-30\,\mathrm{km\,s^{-1}}$. All maps were set to reach approximately the same entropy ($S = -0.02$). Dashed lines indicate the mean and the $\pm 1\sigma$ CIs. The phase shift relative to the pulsar ephemeris is consistent with zero (blue solid line), and the emission feature is significant at a $\sim 4.2\sigma$ level.
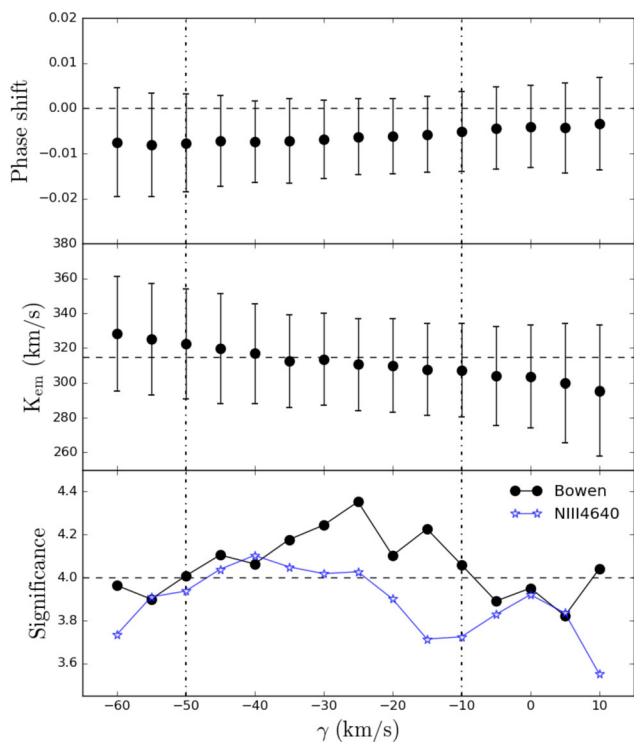
Figure 6. Diagram showing the best-fitting solutions of the phase shift, K_{em} amplitude with bootstrap estimate of 1σ errors and significance level of the donor spot feature derived from Bowen (black filled circles) and N III $\lambda 4640$ (blue stars) maps, as a function of the assumed systemic velocity. Vertical dash–dotted lines mark the preferred range of γ, over which the statistical significance of the secondary feature is greater than 4σ.

$\lambda 4640$ spot, signifying the merit of assigning multiple Bowen transitions to one image. In both cases, the level of significance peaks near the mid-point of the γ range. As a final step in constraining the systemic velocity, we select a range (indicated by vertical dash–dotted lines) over which the significance of the Bowen spot is greater than the 4σ level (horizontal dashed line). Hence, we use the combined Bowen spot and focus only on this final range of γ ($\gamma = -30 \pm 20\,\mathrm{km\,s^{-1}}$) for deriving the RV semi-amplitude.

5.3.2 K_{em} velocity

The middle panel of Fig. 6 shows that within the preferred γ range, K_{em} amplitude is very weakly dependent on the underlying γ assumption, with a maximum of $8\,\mathrm{km\,s^{-1}}$ drift around the central value of $315\,\mathrm{km\,s^{-1}}$ (marked by a horizontal dashed line). We therefore conclude that the systematics due to uncertainties in the main assumption underlying the tomography-based method can be easily tracked down and quantified. At low SNRs, it is clearly the case that the systematic uncertainty due to our assumption of γ is subdominant. Using the information from the diagram, we derive the best estimate of $K_{\mathrm{em}} = 315 \pm 28$ (statistical) ± 8 (systematic) $\mathrm{km\,s^{-1}}$; and $\Delta\phi_{\mathrm{spot}} = -0.006 \pm 0.01$ (statistical) ± 0.001 (systematic).

The strategy described above can be easily extended to mid- to high-SNR cases, as well as cataclysmic variable (CV) systems, where a different emission-line diagnostic is used (e.g. Ca II; van Spaandonk et al. 2010). We will present a reanalysis of the higher SNR Bowen data of other previously published systems (Cornelisse et al. 2008) with updated system parameter constraints in a future paper. Assuming that the emission components coming from the irradiated companion are detected, relevant constraints on true K_2 as well as the binary mass ratio q can be inferred by applying the 'K-correction' to the observed K_{em} amplitude.

6 DISCUSSION

6.1 The *K*-correction

Muñoz-Darias, Casares & Martínez-Pais (2005, hereafter, MCM05) showed that the deviation between the reprocessed light centre and the centre of mass of the Roche lobe-filling donor ($K_c = K_{\mathrm{em}}/K_2 < 1$) has a very weak dependence on the inclination angle i, but is strongly dependent on the mass ratio q and the disc flaring angle α (see MCM05, Fig. 4). With little or no knowledge of the disc shielding parameter, the K-correction is constrained between $\alpha = 0°$ (maximum displacement) and the limit set by emission from the limb of the irradiated region (minimum displacement): $K_{\mathrm{em}}/K_2 < 1 - 0.213\, q^{2/3}(1+q)^{1/3}$.

Using the new analysis toolset, we could also confirm the significance (4.2–4.7σ level) of the He II $\lambda 5411$ spot and the phasing constraint ($\Delta\phi_{\mathrm{spot}} = 0.009 \pm 0.009 \pm 0.002$) points to the inner Roche lobe of the donor star as a possible reprocessing site. However, we derived a velocity semi-amplitude significantly higher (3.3σ) than the Bowen K_{em} velocity: $K_{\mathrm{em,He\,ii}} = 477 \pm 29 \pm 27\,\mathrm{km\,s^{-1}}$. We
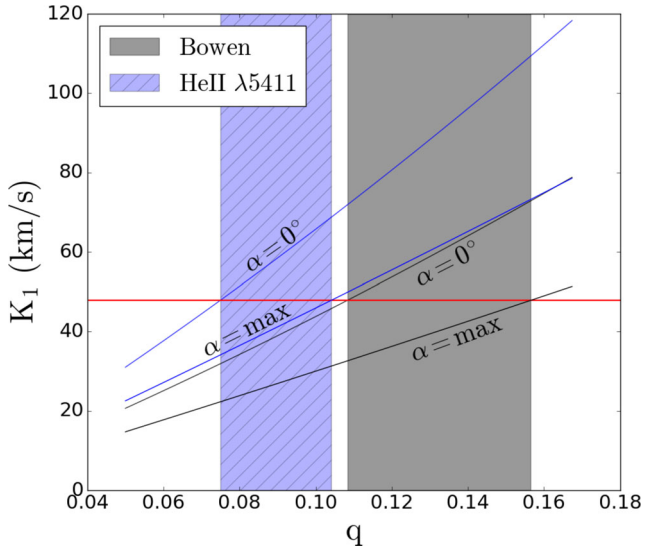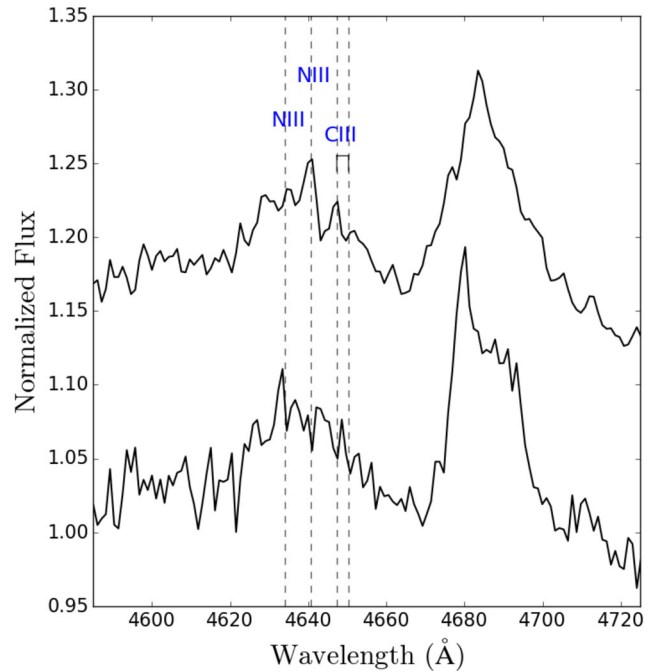
Figure 7. Constraints on q using the K amplitude derived from the Bowen (grey shaded region) and He II λ5411 spot (blue shaded region). The horizontal red line denotes the estimate of K_1 from the pulsar solution.

Figure 8. The Bowen/He II region of the average spectrum in the rest frame of the companion (top) compared with a straight average spectrum (bottom). At least three narrow peaks corresponding to known N III/C III transitions (vertical dashed lines) emerge in the Doppler-corrected average. Top spectrum was calculated using the K_{em} amplitude and the systemic velocity values reported in Table 2.

initially considered whether the He II λ5411 emission component could also come from the irradiated companion, albeit a different region of the Roche lobe – possibly due to differential shielding by the accretion disc. We then used the numerical solution for K_c ($\alpha = 0°$) derived in MCM05, for the lower inclination angle case (deduced from the lack of X-ray eclipses), to perform a K-correction for both K_{em} velocities.

As the velocity amplitude of the NS ($K_1 = 47.848 \pm 0.001\,\mathrm{km\,s^{-1}}$) is accurately known from the pulsar solution, the upper and lower limits for q inferred from the Bowen and the 5411 Å spot can be easily visualized in a K_1–q plane (Fig. 7). Not surprisingly, the two significantly different RVs with their associated errors (by adding the statistical and systematic uncertainties in quadrature) had led to very different constraints of q (denoted by grey and blue shaded regions for the Bowen and He II λ5411 spot, respectively). Since there is no overlap between these shaded areas, there exists no value of q that would satisfy both velocity constraints at the same time, i.e. only one of the two emission spots can originate from the surface of the donor. We must therefore focus on the K_{em} velocity that most certainly traces the orbit of the companion to derive a feasible set of parameter constraints.

Previous studies have shown that the irradiated atmospheres of the companion star in many LMXBs are powerful emitters of the fluorescence N III components. Since we have verified that narrow lines are also present in the Bowen region of J1814, we may, by extension, attribute them to the donor. A further support to this hypothesis is provided by the correct phasing and the >4σ significance level of the relevant spot feature in the reconstructed Doppler map. Similar to most of the other Bowen targets, the strongest component around 4630–4650 Å is N III λ4640, which only becomes visible in the Doppler-corrected average spectrum (Fig. 8). Therefore, we are confident that the grey region ($0.108 < q < 0.157$) in Fig. 7 represents a reliable range of the mass ratio for J1814. Following this argument, we rule out the possibility that the component detected in the 5411 Å emission profile comes from the X-ray illuminated front face of the companion. A tentative scenario for the origin of He II λ5411 emission is proposed in Section 6.4.

6.2 Binary parameter estimation

The detection of Bowen emission lines in J1814 opens up a special opportunity to constrain the RV of the companion star (K_2), and thereby the mass of the accreting millisecond pulsar (M_1) via the mass function equation:

$$f(M) = \frac{K_2^3 P_{orb}}{2\pi G} = \frac{M_1 \sin^3(i)}{(1+q)^2}. \tag{2}$$

The observed lower limit to K_2 ($K_{em} = 315 \pm 29\,\mathrm{km\,s^{-1}}$), combined with the precise determination of K_1, delivers an absolute upper limit to the mass ratio of $q < 0.167$, which implies, using Paczyński's approximation:$\sin(\alpha_{max}) \simeq R_2/a \simeq 0.462 q^{1/3}/(1+q)^{1/3}$ (Paczyński 1971), that the disc opening angle α cannot be higher than ∼14°.

In order to arrive at the most reliable estimation of true K_2, we developed an algorithm to extend the MCM05 numerical solutions for the K-correction to a set of fast fourth-order polynomial approximations:

$$K_c = \frac{K_{em}}{K_2} \simeq N_0 + N_1 q + N_2 q^2 + N_3 q^3 + N_4 q^4, \tag{3}$$

so that α can take any value between 0° and 14°. By interpolating over the grid of K-correction functions (for the $i = 40°$ case and α from 0° to 18° in steps of 2°) provided in MCM05, we can generate reasonable model K-corrections as functions of q for any arbitrary disc opening angle within the given bounds. The best-fitting polynomial can be obtained with the generated model and applied to the measured K_{em} amplitude.

With the measurements of the binary orbital period (P_{orb}) and the projected RV semi-amplitude K_2, equation (2) gives the minimum allowable mass of the compact primary M_1 (as $\sin(i) \lesssim 1$ and

Table 2. XTE J1814-338 system parameters with estimates of $1\sigma/68$ per cent uncertainties.

Parameter	Value
P_{orb} (d)[a]	0.178 110 219(2)
T_0HJD(UTC)[a]	2452798.3539536(9)
γ (km s^{-1})	-30 ± 20
K_{em} (km s^{-1})	315 ± 28 (statistical) ± 8 (systematic)
K_1 (kms^{-1})[b]	47.848 ± 0.001
K_2 (km s^{-1})	390^{+35}_{-36}
q (M_2/M_1)	$0.123^{+0.012}_{-0.010}$
i ($^{\circ}$)	35–78
M_1(M$_{\odot}$)	$2.0^{+0.7}_{-0.5}$
M_2(M$_{\odot}$)	$0.24^{+0.08}_{-0.05}$

Notes. [a]Adapted from (Papitto et al. 2007); [b]Based on (Papitto et al. 2007).

$1 + q > 1$). Precise determinations of stellar masses require knowledge of the mass ratio q as well as the inclination angle i.
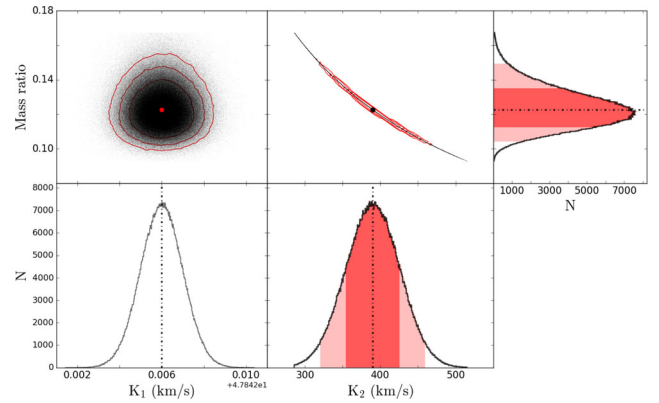
6.2.1 Monte-Carlo analysis

To fully account for uncertainties in all of the observables/input parameters, we performed a Monte Carlo analysis and considered a random distribution of inclination angles to establish the probability density functions (PDFs) of the unknown system parameters. By selecting synthetic K_{em}, K_1 and P_{orb} values from a Gauss-normal distribution (with a mean and 1σ error equal to the observed values; see Table 2), a set of simulated data can be obtained at each Monte Carlo trial and used as inputs to equation (2). Since a firm lower limit on α for J1814 is not known, we chose to let α follow a uniform distribution between 0° and 14°. A value as low as zero is perhaps unlikely given the presence of an active accretion disc, but we prefer not to bias our results by adopting some ad hoc estimate of α. For every combination of randomly generated K_{em}, K_1 and α values (α is a continuous variable), we determined an accurate K-correction for the α angle using the previously developed approximation tool. The updated K_c was then applied to K_{em}, followed by evaluation of the solution for the binary mass ratio ($q = M_2/M_1 = K_1/K_2$) and the corresponding true K_2.

With a set of synthetic q, K_2 and P_{orb} in place, we proceeded to calculate a lower limit to the inclination angle by assuming a maximum stable NS mass of 3.2 M$_{\odot}$. The upper limit to i was simply estimated based on Paczyński's relation given the absence of X-ray eclipses (Krauss et al. 2005). This would result in an overall very loose constraint on the inclination, $35^{\circ} \lesssim i \lesssim 78^{\circ}$. Therefore, during the last step, we used a uniform distribution for $\cos(i)$ (between the lower and upper bounds set by the particular combination of input values) to select a random inclination angle for deriving component masses. The same process was simulated 10^6 times. Finally, the large number of separate outcomes evaluated in individual trials were assembled into PDFs presented in Figs 9 and 10.

6.2.2 The binary mass ratio and component masses

Perhaps the main disadvantage of the Bowen fluorescence technique lies in the fact that the measured K_{em} velocity represents only a solid lower limit to K_2. However, in this case, we have the significant advantage of knowing the RV semi-amplitude of the NS K_1 very accurately. As a result, both K_2 and q PDFs (see Fig. 9)

Figure 9. PDFs of K_2 and q derived from our Monte Carlo analysis (10^6 trials) for $35^{\circ} \le i \le 78^{\circ}$. Dash–dotted lines denote the locations of the median (50th percentile). Red-shaded areas correspond to the regions between the 2.5th and 97.5th percentiles. 68 per cent of the data fall within the darker regions. Best estimates of these system parameters and their associated 1σ errors are given in Table 2.
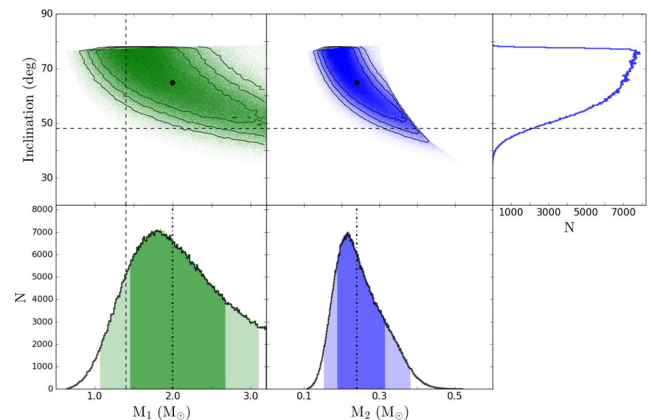

Figure 10. PDFs of the masses of the stellar components. The median values are denoted by dash–dotted lines. As in the previous PDF's, dark/light areas correspond to the regions between the 16th/2.5th and 84th/97.5th percentiles. The canonical value for the NS mass (1.4 M$_{\odot}$), denoted by a vertical dashed line, lies just outside the 68 per cent confidence limits. The horizontal dashed line denotes the lower limit to the inclination angle ($i \gtrsim 48^{\circ}$) for an assumed pulsar mass of 1.4 M$_{\odot}$.

display near-Gaussian distributions under the assumption of randomly distributed inclinations. By propagating the uncertainties in all estimated quantities – including especially the full uncertainty in the opening angle of the accretion disc and the systemic velocity – into the errors in the output quantities, we were able to derive robust estimates of the true velocity semi-amplitude of the donor star and the binary mass ratio (with 1σ errors of less than 10 per cent for both parameters): $K_2 = 390^{+35}_{-36}$ km s^{-1}, $q = 0.123^{+0.012}_{-0.010}$.

Additionally, a lower limit to the inclination for an assumed pulsar mass of 1.4 M$_{\odot}$ can be established ($i \gtrsim 48^{\circ}$) from $K_2 > K_{em} = 315 \pm 29$ km s^{-1}. The most secure constraint on i (as shown in Fig. 10) would be $35^{\circ} < i < 78^{\circ}$, using the knowledge of lack of X-ray dips and combining Bowen K_{em} velocity with $M_1 < 3.2$ M$_{\odot}$. This new inclination constraint thus provides a tighter lower bound compared with previously obtained limits based on burst oscillation properties ($26^{\circ} < i < 50^{\circ}$; Bhattacharyya et al. 2005), or by assuming a magnitude limit ($R > 23.3$) of the companion during quiescence ($22^{\circ} < i < 77^{\circ}$; Krauss et al. 2005).
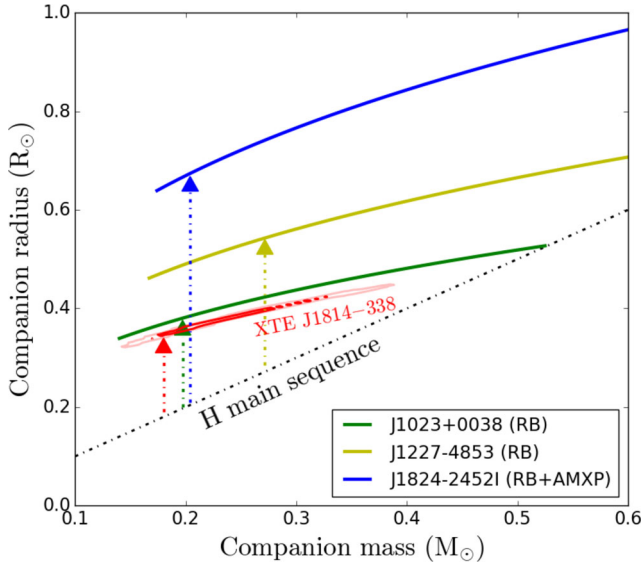
Figure 11. A comparison of the mass–radius relationships for the companion of J1814 and three t-MSPs (so far, all three are redbacks, RBs; see e.g. Archibald et al. 2009; Papitto et al. 2013; Bassa et al. 2014; Stappers et al. 2014) with the approximate relation for ordinary low-mass hydrogen main-sequence stars. The 68 per cent and 95 per cent confidence regions for J1814 (red contours) exclude the mass–radius relation for hydrogen main-sequence stars, indicating that the companion must be bloated. Dash–dotted lines with arrows denote nominal M_2 values determined for a pulsar mass of 1.4 $M_\odot$.

Fig. 10 shows the negative correlation between the inclination and the component masses, M_1 and M_2. The projected 1D PDF of the companion mass (M_2) has a tail extending to 0.38 $M_\odot$ (95 per cent confidence) and a lower 95 per cent confidence limit of 0.15 $M_\odot$, which coincides with the minimum companion mass estimated from the pulsar mass function (Markwardt, Strohmayer & Swank 2003). The 68 per cent CI for M_2 ($0.24^{+0.08}_{-0.05}$ $M_\odot$) is also in excellent agreement with the M_2 constraints deduced from the studies of the quiescent optical counterpart of J1814 (D'Avanzo et al. 2009; Baglio et al. 2013).

The much wider M_1 PDF peaks beyond 1.4 $M_\odot$ ($2.0^{+0.7}_{-0.5}$ $M_\odot$; 68 per cent). We note that the canonical mass of 1.4 $M_\odot$ is not ruled out ($1.1 \lesssim M_1 \lesssim 3.1$; 95 per cent) with the lack of knowledge of i, and that a canonical NS mass would be more compatible with a relatively high inclination angle ($63° \lesssim i \lesssim 76°$; 68 per cent). We already know that extremely high-mass NSs exist from the precise determinations of the mass of two radio millisecond pulsars, PSR J1614−2230 ($M_1 = 1.928 \pm 0.017$ $M_\odot$; Demorest et al. 2010; see also Fonseca et al. 2016) and PSR J0348+0432 ($M_1 = 2.01 \pm 0.04$ $M_\odot$; Antoniadis et al. 2013). An improvement in the measurement of the binary inclination is the key factor in achieving a tighter M_1 constraint for J1814, which may have the potential to exclude some soft equations of state. A summary of system parameters with estimates of 1σ uncertainties is given in Table 2.

6.3 The nature of the companion

Fig. 11 compares the mass–radius contours (showing the 68 per cent and 95 per cent confidence regions) for a Roche lobe-filling donor in a 4.275 h binary (J1814) with the approximate relation for ordinary low-mass hydrogen main-sequence stars (using $R/R_\odot = M/M_\odot$;

black dash–dotted line). Our dynamical mass constraints confirmed previous suggestions of a main-sequence M-type companion in J1814, and that the companion is likely significantly bloated (given the 68 per cent/95 per cent confidence regions) presumably due to X-ray heating by an accretion-powered millisecond pulsar (see also Bhattacharyya et al. 2005; Krauss et al. 2005).

The fact that the radius of the secondary is $\approx$ 90 per cent larger than expected (assuming $M_2 = 0.18$ $M_\odot$ for a 1.4 $M_\odot$ NS) is reminiscent of the first known transitional millisecond pulsar binary (t-MSP) PSR J1023+0038 (Archibald et al. 2009). This archetypal redback system (an eclipsing binary MSP with a companion of $\gtrsim 0.1$ $M_\odot$; Roberts 2011) in the Galactic field has a similar orbital period to J1814 (green mass–radius curve in Fig. 11) and a main sequence-like, similar mass companion ($\sim$0.2 $M_\odot$) that is bloated to $\approx$1.9 times the expected radius. Given these remarkable similarities, it is intriguing to speculate that before the 2003 outburst, the companion of XTE J1814-338 may have been irradiated by a rotation-powered ('recycled') redback-like pulsar that switches on during an X-ray quiescent state. Ablation processes driven by the pulsar spin-down power could bloat the secondary star significantly.

6.4 A hidden 'redback'?

Evidence has been built over the past two decades to indicate strongly irradiated companions of several AMXP systems during quiescence. Optical light curves of SAX J1808.4-3658, IGR J00291+5934 and XTE J1814-338 all showed large-amplitude, sinusoidal modulations at the known orbital period (Homer et al. 2001; Campana et al. 2004; D'Avanzo et al. 2007, 2009). As first pointed out by Burderi et al. (2003), the irradiating luminosity necessary to account for the observed optical flux is about two orders of magnitude higher than the quiescent X-ray luminosity L_X ($\lesssim 10^{32}$ ergs^{-1}). On the other hand, the release of rotational energy via a relativistic particle wind (the spin-down luminosity; $L_{sd} \sim 10^{34}$ erg s^{-1}) by a reactivated radio pulsar would be sufficient to illuminate the companion (Hartman et al. 2008).

From fitting multiband, quiescent optical light curves of J1814 using a model for an irradiated secondary, Baglio et al. (2013) noted an apparent discrepancy between the inferred value of M_2 (consistent with the companion being an M-type main-sequence star) and the day-side surface temperature of the companion ($\sim$5500 K), which is typical of an earlier spectral type (G- or K-type) star (see also D'Avanzo et al. 2009). By assuming that the relativistic wind of an active radio pulsar irradiates the companion and increases its surface temperature, an estimate of the irradiation luminosity, $L_{irr} = \sigma_{SB}\left(T_{day}^4 - T_{night}^4\right)$, can be related to the pulsar's spin-down energy as $L_{sd} = 4\pi a^2 L_{irr}/\epsilon_{irr}$, where σ_{SB} is the Stefan–Boltzmann constant, a is the orbital separation and ϵ_{irr} is the irradiation efficiency. For an efficiency in the range of 0.1–0.3 typical of irradiated black widow ($M_2 << 0.1$ $M_\odot$) and redback MSP systems (Breton et al. 2013), the derived value of L_{sd} ($\sim [6–17] \times 10^{34}$ erg s^{-1}) is consistent with the spin-down luminosity of a 3.2 ms pulsar (Baglio et al. 2013). This finding, combined with the new dynamical mass constraints and the bloated nature of the companion (see Section 6.3 and Fig. 11), provides indirect evidence of a redback MSP during quiescence in XTE J1814-338 (although no evidence of pulsed radio emission of this source has been reported to date).

The presence of a redback MSP might shed some light on the emission spot seen in the Doppler map of He II λ5411 in Fig. 4. Since its V_y-coordinate is larger than the upper limit to K_2 derived from the N III λ4640/Bowen spot, it cannot be produced on the irradiated

surface of the donor. Noticeable differences between the shape (or FWHM) of the He II $\lambda5411$ and the N III $\lambda4640$ spot suggest that the former might instead arise from a more extended structure, perhaps an intra-binary shock caused by the pulsar wind interacting with the ablated material from the donor. A puzzling behaviour that may be explained by the presence of a shock front was also noted by D'Avanzo et al. (2009). Quiescent optical light curves of J1814 exhibit a decrease in the *V*-band flux between phase 0.05 and 0.17. The deep minimum around phase 0 (inferior conjunction of the donor star) is likely caused by a shock front eclipsing a residual accretion disc if present during quiescence, as suggested in Baglio et al. (2013).

7 CONCLUSIONS

We have presented the first detection of the donor star in the AMXP XTE J1814-338 using Doppler tomography of the Bowen region ($\lambda\lambda4630$–50) inspired by our earlier studies of Sco X-1 (Steeghs & Casares 2002) as well as a number of LMXBs in active states (Cornelisse et al. 2008). The reconstructed Bowen Doppler map reveals a compact spot at phase 0 and $V_y \sim 315\,\mathrm{km\,s^{-1}}$, which has been interpreted as possible evidence of emission from the irradiated donor. In the lowest SNR regime, we used a bootstrap Monte Carlo test to quantify the significance of the Bowen spot from ensembles of maps. The spot is statistically significant ($>4\sigma$), and at the expected position of the donor star, thus providing a unique opportunity to constrain the RV semi-amplitude of the companion of an AMXP.

Since the Bowen components originate from the front face of the donor, the velocity semi-amplitude (K_{em}) derived from the Bowen spot must be biased towards lower values. Based on the numerical solutions for $K_c = K_{\mathrm{em}}/K_2$ (MCM05), we developed an algorithm to compute synthetic *K*-corrections as functions of the mass ratio q for any arbitrary disc opening angle α between $0°$ and $18°$, which can be applied to K_{em} to get true K_2. To account for uncertainties in all of the input parameters, we performed a Monte Carlo analysis and considered a random distribution of inclination angles to establish the PDFs of the binary parameters. Under the most conservative scenario, we have the following constraints: $q = 0.123^{+0.012}_{-0.010}$; $35° < i < 78°$; $1.5\,\mathrm{M_\odot} < M_1 < 2.7\,\mathrm{M_\odot}$; $0.19\,\mathrm{M_\odot} < M_2 < 0.32\,\mathrm{M_\odot}$ (68 per cent).

The new dynamical mass constraints confirmed previous suggestions that the companion is a significantly bloated, main-sequence M-type star. Furthermore, a VLT campaign carried out between 2004 and 2009 (during quiescence) gave indications of a strongly irradiated companion that is heated by the relativistic particle wind of a rotation-powered MSP (D'Avanzo et al. 2009; Baglio et al. 2013). The presence of a redback-like MSP ($M_2 \sim 0.2$) might also explain the puzzling emission feature seen in the He II $\lambda5411$ Doppler map, which likely originates from an intra-binary shock created from the interaction between the pulsar wind and the ablated material from the companion.

REFERENCES

Alpar M. A., Cheng A. F., Ruderman M. A., Shaham J., 1982, Nature, 300, 728

Antoniadis J. et al., 2013, Science, 340, 448

Archibald A. M. et al., 2009, Science, 324, 1411

Backer D. C., Kulkarni S. R., Heiles C., Davis M. M., Goss W. M., 1982, Nature, 300, 615

Baglio M. C., D'Avanzo P., Muñoz-Darias T., Breton R. P., Campana S., 2013, A&A, 559, A42

Bassa C. G. et al., 2014, MNRAS, 441, 1825

Bhattacharyya S., Strohmayer T. E., Miller M. C., Markwardt C. B., 2005, ApJ, 619, 483

Breton R. P. et al., 2013, ApJ, 769, 108

Burderi L., Di Salvo T., D'Antona F., Robba N. R., Testa V., 2003, A&A, 404, L43

Campana S. et al., 2004, ApJ, 614, L49

Casares J., Steeghs D., Hynes R. I., Charles P. A., O'Brien K., 2003, ApJ, 590, 1041

Cornelisse R., Casares J., Muñoz-Darias T., Steeghs D., Charles P., Hynes R., O'Brien K., Barnes A., 2008, in Bandyopadhyay R. M., Wachter S., Gelino D., Gelino C. R., eds, AIP Conf. Ser. Vol. 1010, A Population Explosion: The Nature & Evolution of X-ray Binaries in Diverse Environments. Am. Inst. Phys., New York, p. 148

Cornelisse R. et al., 2009, A&A, 495, L1

D'Avanzo P., Campana S., Covino S., Israel G. L., Stella L., Andreuzzi G., 2007, A&A, 472, 881

D'Avanzo P., Campana S., Casares J., Covino S., Israel G. L., Stella L., 2009, A&A, 508, 297

de Martino D. et al., 2014, MNRAS, 444, 3004

Demorest P. B., Pennucci T., Ransom S. M., Roberts M. S. E., Hessels J. W. T., 2010, Nature, 467, 1081

Efron B., Tibshirani R. J., 1993, An Introduction to the Bootstrap. Chapman & Hall, New York

Fonseca E. et al., 2016, ApJ, 832, 167

Hartman J. M. et al., 2008, ApJ, 675, 1468

Homer L., Charles P. A., Chakrabarty D., van Zyl L., 2001, MNRAS, 325, 1471

Horne K., 1986, PASP, 98, 609

Hynes R. I., Steeghs D., Casares J., Charles P. A., O'Brien K., 2003, ApJ, 583, L95

Jonker P. G. et al., 2003, MNRAS, 344, 201

Krauss M. I. et al., 2005, ApJ, 627, 910

Longa-Peña P., Steeghs D., Marsh T., 2015, MNRAS, 447, 149

McClintock J. E., Canizares C. R., Tarter C. B., 1975, ApJ, 198, 641

Manser C. J. et al., 2016, MNRAS, 455, 4467

Markwardt C. B., Swank J. H., 2003, IAU Circ., 8144, 1

Markwardt C. B., Strohmayer T. E., Swank J. H., 2003, Astron. Telegram, 164, 1

Marsh T. R., 2001, in Boffin H. M. J., Steeghs D., Cuypers J., eds, Lecture Notes in Physics, Vol. 573, Astrotomography, Indirect Imaging Methods in Observational Astronomy. Springer Verlag, Berlin, p. 1

Marsh T. R., Horne K., 1988, MNRAS, 235, 269

Muñoz-Darias T., Casares J., Martínez-Pais I. G., 2005, ApJ, 635, 502 (MCM05)

Paczyński B., 1971, ARA&A, 9, 183

Papitto A., di Salvo T., Burderi L., Menna M. T., Lavagetto G., Riggio A., 2007, MNRAS, 375, 971

Papitto A. et al., 2013, Nature, 501, 517

Patruno A., Watts A. L., 2012, preprint (arXiv:1206.2727)

Roberts M. S. E., 2011, in Burgay M., D'Amico N., Esposito P., Pellizzoni A., Possenti A., eds, AIP Conf. Ser. Vol. 1357, Radio Pulsars: An

Astrophysical Key to Unlock the Secrets of the Universe. Am. Inst. Phys., New York, p. 127–130.

Roy J. et al., 2015, ApJ, 800, L12

Schneider D. P., Young P., 1980, ApJ, 238, 946

Shafter A. W., 1985, in Lamb D. Q., Patterson J., eds, Cataclysmic Variables and Low-Mass X-ray Binaries. Reidel, Dordrecht, p. 355

Stappers B. W. et al., 2014, ApJ, 790, 39

Steeghs D., 2003a, MNRAS, 344, 448

Steeghs D., 2003b, IAU Circ., 8155, 2

Steeghs D., Casares J., 2002, ApJ, 568, 273

Strohmayer T. E., Markwardt C. B., Swank J. H., in't Zand J., 2003, ApJ, 596, L67

van Spaandonk L., Steeghs D., Marsh T. R., Torres M. A. P., 2010, MNRAS, 401, 1857

Watson C. A., Dhillon V. S., 2001, MNRAS, 326, 67

Watts A. L., Strohmayer T. E., Markwardt C. B., 2005, ApJ, 634, 547

Wijnands R., van der Klis M., 1998, Nature, 394, 344

This paper has been typeset from a TEX/LATEX file prepared by the author.